CHAPTER V

RESULTS AND DISCUSSION

In this chapter we will report and discuss the results of the growth of CIGS films by the two-stage or CURO process and the modified two-stage or CUPRO process. Both processes have the *in situ* monitoring of signals during the growth. The crystal structure and the morphology of the CIGS films grown by the CURO process will be characterized and the growth model of these films will be proposed. The cell performances will also be characterized using a standard current-voltage measurement system and a quantum efficiency measurement system.

For the CUPRO process, we will focus on the details of the growth process and the effects of the process parameters, such as substrate temperatures, crystal orientation of the CIGS film etc. The five-stage growth model for the CIGS film grown by the CUPRO process then will be proposed and the cell performances will be presented using the same standard measurement.

5.1 Results and Discussion of the CIGS Films Grown by CURO Process and the Cell Performances

5.1.1 *in situ* Monitoring of the Growth of CIGS Thin Films: EPD based T_{pyro}, T_{sub} and OP

Figure 5.1 shows typical temperature profiles of Cu, In, Ga sources and the evolution of the calculated content of Cu; y_{cal} = [Cu]/([In]+[Ga]), of the growing film for the CURO process. The parameter y_{cal} can be expressed as

$$y_{cal}(t) = \frac{y(t_1)}{t} \cdot t_1 \qquad \text{for } t \geq t_1 \quad . \qquad (5.1)$$

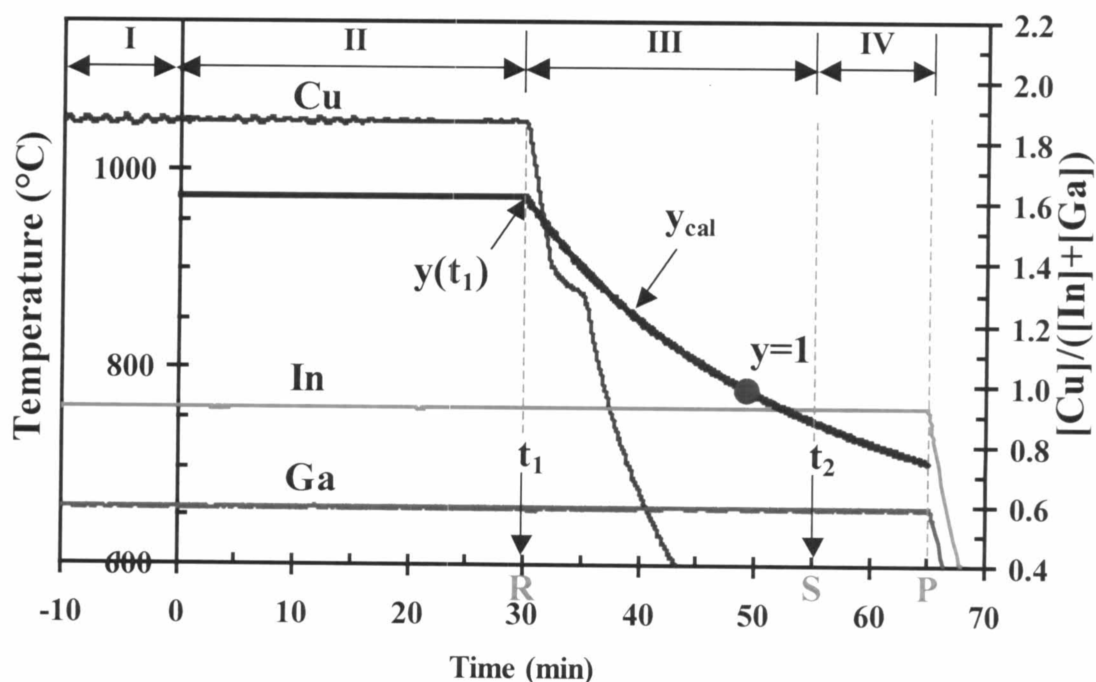

Figure 5.1: Typical temperature profiles of Cu, In, Ga sources and calculated content of Cu (y_{cal}) of the growing film for the CURO process.

During the process, the temperatures of the substrate and Se source were fixed at 500°C (before opening the shutter) and 260°C, respectively. The temperatures for other sources were chosen for total film thickness of approximately 3 μm and for total deposition time of 65 minutes. We can distinguish our deposition process into four states. The first state (I) is before the opening of the shutter ($t<0$). The second state (II) is the accumulation of Cu-rich film ($y>1$). The third state (III) is the conversion from Cu-rich to EPD (at t_2). The fourth (IV) is the Cu-poor CIGS film ($y<1$) until the process is stopped. The calculated Cu content is equal to 1.6 during the second state. At the end of the second state ($t=t_1$), the Cu source is turned off, the Cu flux rapidly falls to zero and the film evolves from Cu-rich to Cu-poor composition.

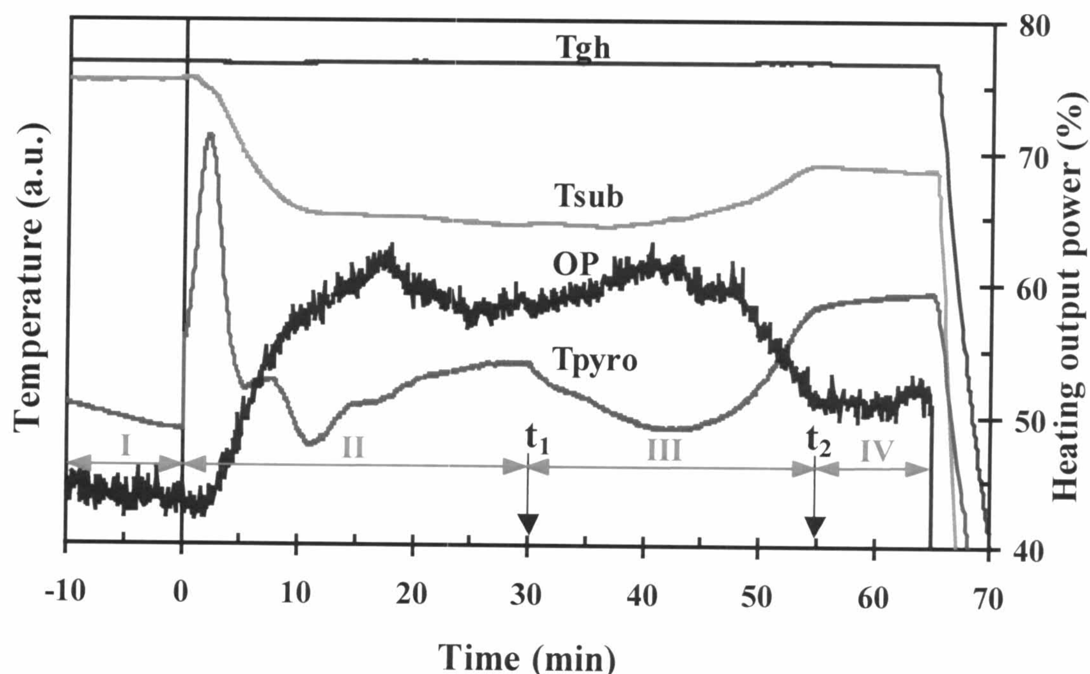

Figure 5.2: The *in situ* monitoring signals of the temperatures profiles in Fig 5.1.

The *in situ* monitoring signals during the growth process are shown in Fig. 5.2. These signals show typical variations of the sample surface temperature, as detected by the pyrometer (T_{pyro}), the substrate temperature (T_{sub}), as detected by a thermocouple at the back surface of the glass substrate and the output power (OP) of the temperature controller which keeps the graphite heater at a constant temperature (T_{gh}).

During the period of state I when the shutter is still closed, all signals are in a steady state. At state II when the shutter is opened and the growth process begins, all 3 monitoring signals, T_{pyro}, T_{sub} and OP, start to vary. A sudden jump of the pyrometer signal T_{pyro} at the beginning of the growth process is due to the surface radiation from the substrate and the reflected radiation from the Cu source. When the Cu-rich CIGS film starts to grow, the pyrometer signal T_{pyro} rapidly increases to a certain value and then decreases to become a sharp peak which is followed by a few period of weak oscillations. This sharp peak and the oscillations of T_{pyro} are the result of the optical interference by thin film of the 1.55 μm radiation which is detected by the pyrometer. Due to the poor transparency of the film at this wavelength, the interference disappears as the thickness of the film increases. At large thickness of the Cu-rich CIGS film, the pyrometer signal T_{pyro} shows a steady increase to reach a certain equilibrium value at the end of state II. When the Cu-rich film starts to grow on the front surface, the monitoring substrate temperature, T_{sub}, which is detected on the back surface decreases slowly to an equilibrium temperature. The decrease in the substrate temperature is caused by the increase of the emissivity of the Cu-rich CIGS film due to the segregation of the liquid phase of the Cu_xSe compound [38]. We expect that the Cu_xSe phase exists on the surface of the film and between the CIGS grain boundary as proposed in [11, 49]. As a result

of the lowering of the substrate temperature, the rate of heat transfer from the graphite heater to the substrate increases substantially. As a consequence, in order to keep the temperature of the graphite heater at a constant temperature, output power of the controller must be increased. This is clearly observed from the OP monitoring signal.

At state III, when the Cu source is turned off, reflected radiation from the Cu source reaching the pyrometer decreases accordingly. The pyrometer signal, T_{pyro}, shows a rapid drop to a certain minimum value. The growth of the CIGS film without Cu flux in state III is solely achieved by In, Ga, Se fluxes and Cu from the segregated Cu_xSe phase. On the expense of the Cu_xSe phase in the Cu-rich CIGS film, one would expect the decrease in the emissivity of the surface and the rise in the film temperature. This effect can be observed by the increase of the T_{pyro} signal and the substrate temperature, T_{sub}. Both signals increase in a similar manner up to a rather sharp knee and a flat plateau of the Cu-poor CIGS film. During the same period of time, the increase of the substrate temperature causes a decrease of the output power supplied to the graphite heater. The decrease of this output power is shown by the decrease of the OP signal together with the sharp corner and the flat plateau of the Cu-poor film. Incidentally, both sharp knees of the pyrometer signal and substrate temperature, including the sharp corner of the output power, occur almost at the same position of the time scale. We attribute these transitions of the three monitoring curves to the point indicating that the CIGS film has been completely transformed to the Cu-poor stage. The composition of the CIGS film which is ended at this point has been analyzed by the EDS technique to be $y \approx 0.9$. In this case, we may assign this point to be the end point for the growth process.

5.1.2 Crystal Structure of the Films Grown by CURO Process

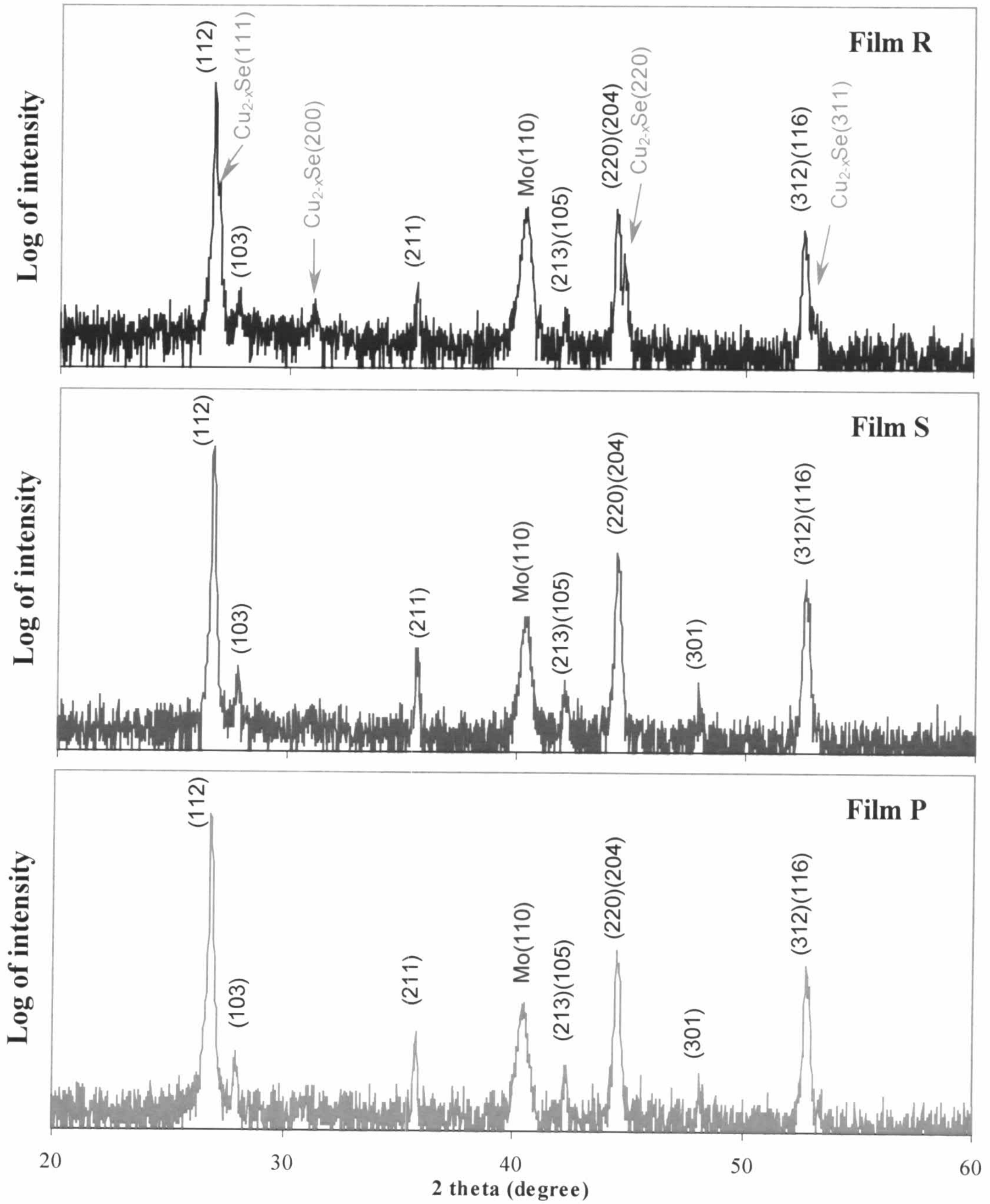

Figure 5.3: XRD spectra of the films R, S and P represent the evolution of CURO growth at the end of states II, III and IV, respectively.

Figure 5.3 shows the typical X-ray diffraction patterns of the films R, S, and P that represent the evolution of the film grown during the CURO process as shown in Fig. 5.1. These films were grown at the same set of temperatures of substrate and Cu, In, Ga, Se sources but ended at different growing time as indicated in Fig. 5.1.

The film R represents the uniform Cu-rich film ended at $t_1 = 30$ min with $y \approx 1.6$, the initial content of Cu used in the CURO process. The film S and P were ended at $t = t_2 = 55$ min and $t = 65$ min, respectively. The film S is the result of a completed CURO process at EPD with $y \approx 0.9$ (desired Cu-deficient). The film P is the result of an extended CURO process with $y \approx 0.75$ (extended Cu-poor). For the content of Ga, all of these films have approximately the same composition of Ga, ([Ga]/([In]+[Ga]) $\approx$ 0.15), as determined by the EDS technique.

These typical XRD spectra show well-defined peaks suggesting that the samples have almost perfect crystal structure. Using the standard JCPDS (Joint Committee on Powder Diffraction Standards) cards to analyze the structural property, all of these films are in agreement with the diffraction lines in the chalcopyrite structure. The pattern of the film R is observed to be the mixed phase between a chalcopyrite phase $CuIn_{1-x}Ga_xSe_2$ and a $Cu_{2-x}Se$ phase. All of the observed peak positions for the $Cu_{2-x}Se$ phase match the berzelianite (JCPDS: 6-680), with $x \approx 0.15$ which belongs to the cubic system with a= 5.739Å, due to reflections from (111), (200), (220) and (311) planes of the reported structure [50]. The presence of the additional phase $Cu_{2-x}Se$ in Cu-rich film is consistent with compositional measurements made using EDS. However, this phase has not been found in both films S and P. This is

confirmed that this phase has been completely converted to single chalcopyrite phase. The comparison between film S and P shows that these two patterns are similar to the standard chalcopyrite phase $CuIn_{1-x}Ga_xSe_2$, except that all other peaks related to the chalcopyrite structure in film P were shifted to higher angle. The shifted pattern can be resulted from the ordered vacancy compound (OVC) or defect-chalcopyrite, which has the lattice spacing smaller than those of chalcopyrite phase [51, 52].

Table 5.1: Calculated values of a, c, c/a and z from the XRD patterns of the films R, S and P shown in Fig. 5.3 and JCPDS for $CuIn_{1-x}Ga_xSe_2$ where $x = 0$, 0.25 and 0.4.

Sample	a (Å)	c (Å)	c/a	z	qualified as:
$CuInSe_2$*	5.782	11.619	2.010	2.4	Random
$CuIn_{0.75}Ga_{0.25}Se_2$*	5.744	11.484	1.999	2.5	Random
$CuIn_{0.60}Ga_{0.40}Se_2$*	5.718	11.390	1.992	2.5	Random
Film R	5.769	11.536	2.000	11.3	textured (112)
Film S	5.768	11.536	2.000	7.3	textured (112)
Film P	5.753	11.506	2.000	13.1	textured (112)

*JCPDS: 40-1488, for $CuIn_{1-x}Ga_xSe_2$ where $x = 0$, 0.25 and 0.40 [53].

The orientation ratio, z = I(112)/I(220)(204), of these films is considered to be comparable to that of the standard powder from bulk JCPDS. The lattice parameters a, c and c/a were also determined and shown in Table 5.1. In comparison of the results for the films R, S, and P, it is seen that the structural

evolution of the film during the CURO growth is typically (112) orientation parallel to the substrate. All of these crystal parameters show the tetragonal structure without a distortion. However, the film P grown with extended decrease of Cu content and ended after EPD shows the decrease of lattice constants both a and c. Thus, as indicated by the phase diagram of the Cu_2Se-In_2Se_3 system in Section 2.1, film P with chalcopyrite structure can tolerate an excess of several percent of $(In,Ga)_2Se_3$ over Cu_2Se without precipitation of extra diffraction peaks (i.e. (002),(110),(200)(004),(202) and (114)) caused by the ordering of vacancies in the defect-chalcopyrite structure [54,55].

5.1.3 Morphology of the Films Grown by CURO Process

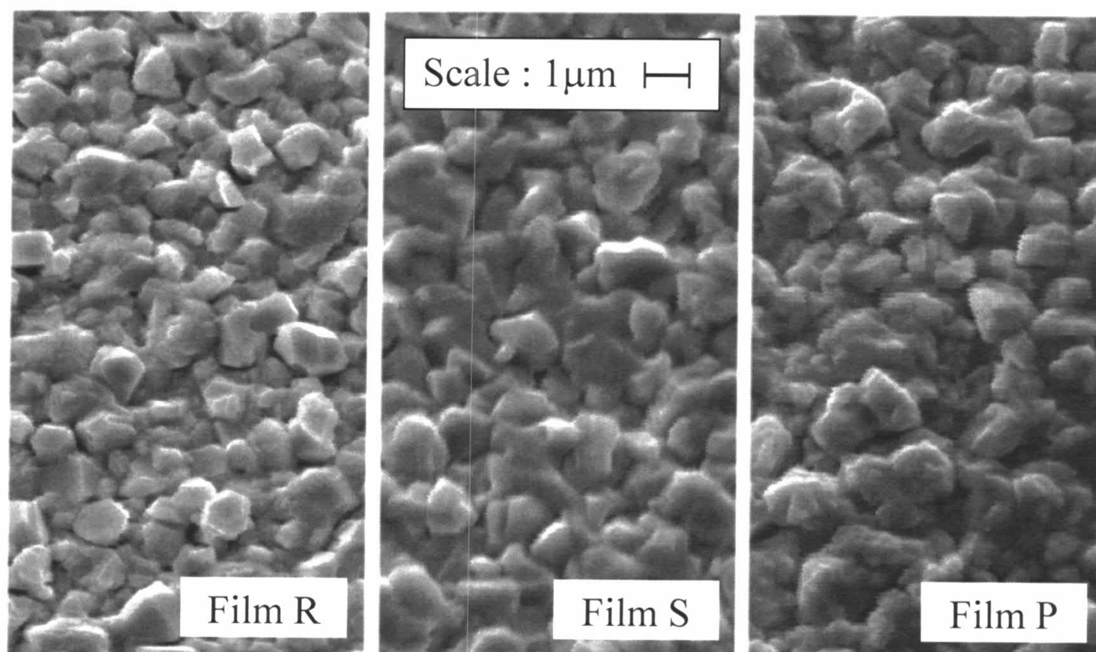

Figure 5.4: SEM micrographs (surface) of the films R, S and P represent the evolution of CURO growth at the end of states II, III and IV, respectively.

Figure 5.4 shows the typical surface morphology of the films R, S, and P that represent the evolution of the film growth during the CURO process as shown in Fig. 5.1. All these polycrystalline films show homogeneous surfaces with average grain sizes of about 1 to 1.5 μm.

Film R represents the uniform Cu-rich film with $y \approx 1.6$ at the end of state II. Its morphology shows the dense grain packing which contains the mixed phase system of the $Cu(In,Ga)Se_2$ and $Cu_{2-x}Se$ as identified in the XRD result. As previous reports [11,38,39], the liquid phase of Cu_xSe compound is expected to be found at the surface of the growing film and between the grain boundaries. The binary phases segregate almost completely at grain surfaces while the grain themselves are nearly stoichiometric with none or minor copper chalcogenide inclusions. To date, there does not exist any direct evidence of a liquid Cu_xSe phase during the growth or of a solid CuSe phase upon cooling in the Cu-rich film. In a series of the surface morphology, both films S and P show the similar grain sizes but slightly larger than that of film R. While the content of Cu decreases from the nearly stoichiometric with $y \approx 0.9$ to the extended Cu-poor with $y \approx 0.75$, the ordered vacancy compound or defect-chalcopyrite would be expected to form from the top part of the growing film.

To study the grain growth mechanism of the completed CURO process at EPD, the cleaved cross-section of film S was carried out. Figure 5.5 is a SEM micrograph of the film S showing the typical grain growth with the rougher surfaces, the columnar shape and the deep crevices between the CIGS grain boundaries at the top fraction of the film. For the bottom fraction of the film, it is dense without void.

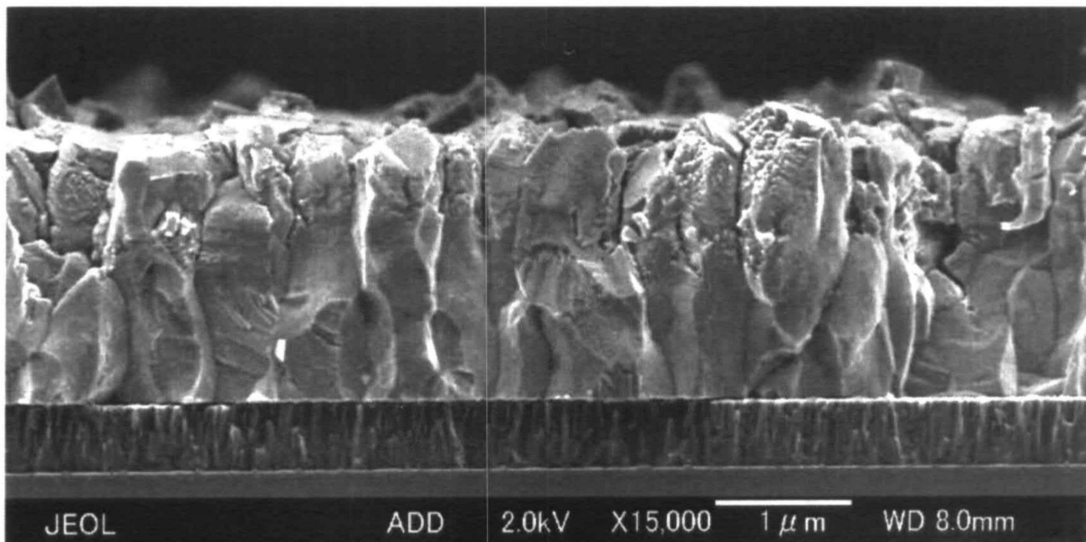

Figure 5.5: SEM micrograph (cross-section) of the film S at $y \approx 0.9$ (EPD) as shown in Fig. 5.1.

These observations can be explained in a straightforward manner only if an active role of the secondary phase in the growth is assumed. The influence of the liquid Cu_xSe phase in Cu-rich film is to induce large, nearly stoichiometric chalcopyrite grains with high structural perfection and good electronic properties [39]. The presence of Cu_xSe on the surface acts as "flux" with a high diffusion coefficient for atomic species involved in the growth process, explaining the success of Cu-poor onto Cu-rich type process. It is important to convert the secondary phase towards the end of the process without affecting the good properties of already grown chalcopyrite. A model for the growth of high quality CIGS thin films using CURO process will be presented in Section 5.1.4.

5.1.4 Growth Model for CURO Process

A growth model is proposed to explain these results for the growth of CIGS thin films by typical two-stage or CURO process. The objective is to understand the growth mechanism of CIGS thin film growing at T_{sub}= 500°C. According to Tuttle *et al.* [38] the formation chemistry is described from the perspective of physical vapor deposition (PVD). In Fig. 5.6, the model qualitatively described the process for the formation of Cu-rich $CuInSe_2$, $Cu(In,Ga)Se_2$ and $CuGaSe_2$. The intent of the Cu-rich stage is to produce a mixed phase of $Cu(In,Ga)Se_2$ and Cu_xSe. The following reaction applies

For $\gamma \geq 1$,

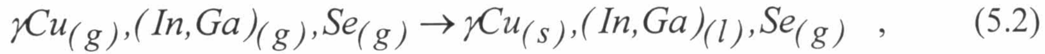

$$\gamma Cu_{(g)}, (In,Ga)_{(g)}, Se_{(g)} \rightarrow \gamma Cu_{(s)}, (In,Ga)_{(l)}, Se_{(g)} \quad , \qquad (5.2)$$

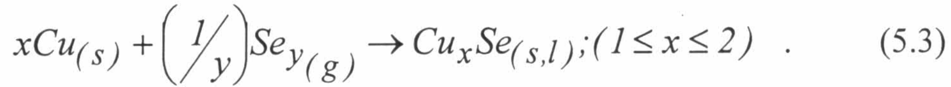

$$xCu_{(s)} + \left(\frac{1}{y} \right) Se_{y(g)} \rightarrow Cu_xSe_{(s,l)}; (1 \leq x \leq 2) \quad . \qquad (5.3)$$

For $T_{sub} \geq 523$°C,

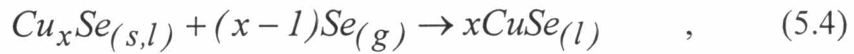

$$Cu_xSe_{(s,l)} + (x-1)Se_{(g)} \rightarrow xCuSe_{(l)} \quad , \qquad (5.4)$$

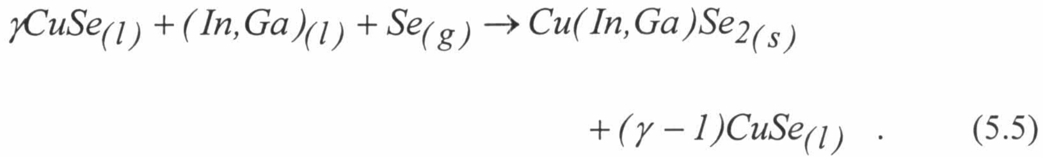

$$\gamma CuSe_{(l)} + (In,Ga)_{(l)} + Se_{(g)} \rightarrow Cu(In,Ga)Se_{2(s)} + (\gamma - 1)CuSe_{(l)} \quad . \qquad (5.5)$$

Upon cooling,

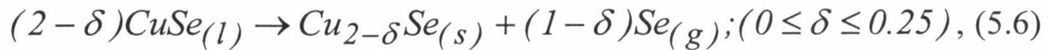

$$(2-\delta)CuSe_{(l)} \rightarrow Cu_{2-\delta}Se_{(s)} + (1-\delta)Se_{(g)}; (0 \leq \delta \leq 0.25), \qquad (5.6)$$

where x in Cu_xSe of Eqs. (5.3) and (5.4) signifies the variable composition of the Cu-Se binary during growth, and δ in $Cu_{2-\delta}Se$ of Eq. (5.6) represents a specific phase identified by XRD.

In Eq. (5.2), Cu and (In,Ga) metals are the only constituents to accommodate on the surface of the substrate at 500°C. It was previously believed that each metal would be subsequently selenized, in the presence of Se vapor, into Cu_xSe and $(In,Ga)_ySe$ binaries, followed by the formation of $Cu(In,Ga)Se_2$ from the binaries. The reaction rates of Cu and In in the presence of Se vapor indicate that the Cu selenizes faster than In. In the presence of over pressure of Se and at substrate temperature in excess of 500°C, the formation of the liquid CuSe phase occurs according to Eq. (5.4). Therefore, it appears that the growth of the ternary $Cu(In,Ga)Se_2$ proceeds in a liquid environment of the excess Cu_xSe binary phase. This accounts for the observed enhanced-grain nature of the aggregated mixture.

The compound formation may now readily proceed according to Eq. (5.5), which is thermodynamically more favorable than the reaction between the Cu-Se and (In,Ga)-Se binaries according to calculations made by Albin *et al.* [56]. If the film is cooled, the liquid CuSe phase would loose Se according to Eq. (5.6), leaving the $Cu_{2-\delta}Se$ solid phase. This phase has been detected by XRD and its presence is consistent with the compositional analysis by EDS.

As illustrated in Fig. 5.6, the subsequent stages of film growth are a combination of reaction chemistry and film formation dynamics. The liquid (Cu_xSe)-solid $(Cu(In,Ga)Se_2)$ phase separation occurs parallel to the substrate plane during the Cu-rich stage. As the $Cu(In,Ga)Se_2$ solid coalesces, the surface

tension between the liquid and solid phases increases and reaches a critical value, at which time the phase separation transforms to an orientation normal to the substrate plane. The Cu_xSe with a layered structure is at the surface of the growing film. This facilitates the conversion of the Cu_xSe to $Cu(In,Ga)Se_2$ during subsequent processing.

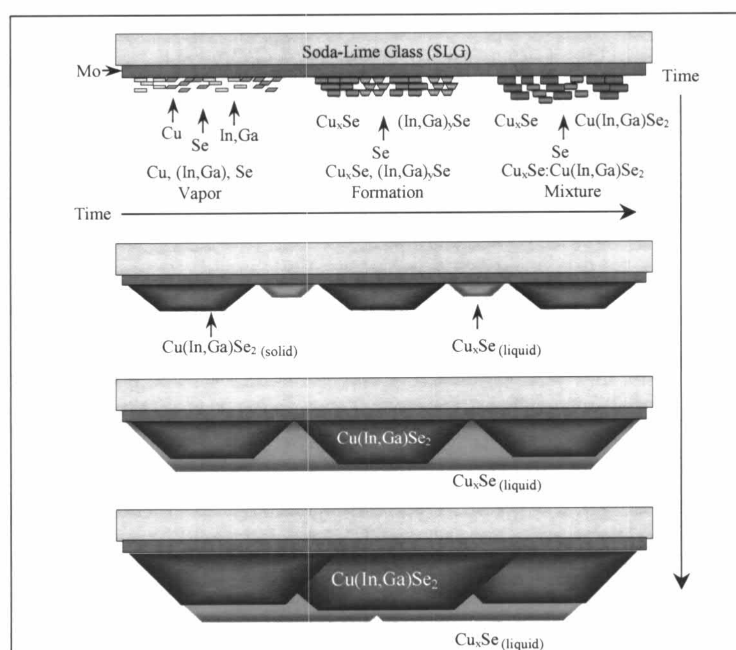

Figure 5.6: Growth model for Cu-rich $Cu(In,Ga)Se_2$ by two-stage or CURO process with the presence of a copper chalcogenide phase [38].

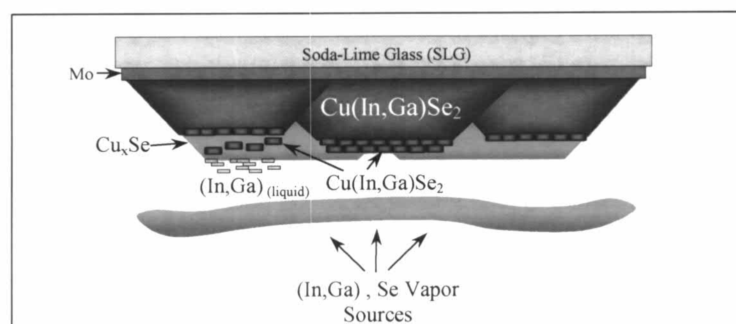

Figure 5.7: Growth model for the conversion of Cu_xSe into $Cu(In,Ga)Se_2$ by exposure to an (In,Ga)-rich vapor trail [38].

In Fig. 5.7, after the Cu source is turned off, the process involes the conversion of Cu_xSe to $Cu(In,Ga)Se_2$. This stage requires an (In,Ga)-rich to consume the excess liquid Cu_xSe by the equivalent reaction chemistry as described in Eqs. (5.7) and (5.8). The presence of a liquid Cu_xSe phase simplifies the diffusion/transport and reaction kinetic issues discussed earlier. The $Cu(In,Ga)Se_2$ is formed near the top surface and transported into a Cu_xSe:$Cu(In,Ga)Se_2$ (liquid-solid) interface, where the growth continues on the solid surface. The continuity of the $Cu(In,Ga)Se_2$ crystallite normal to the substrate plane, as observed in morphological studies, is consistent with such a growth mechanism (large columnar grain).

$$(In,Ga)_{(g)}, Se_{(g)} \rightarrow (In,Ga)_{(l)}, Se_{(g)} \quad , \qquad (5.7)$$

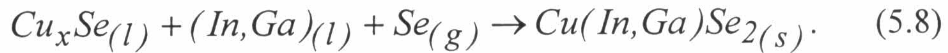

$$Cu_xSe_{(l)} + (In,Ga)_{(l)} + Se_{(g)} \rightarrow Cu(In,Ga)Se_{2(s)} . \qquad (5.8)$$

As the conversion process nears completion, the surface coverage of liquid Cu_xSe is incomplete and solid regions with a surface composition of the ordered vacancy compound (OVC) or defect-chalcopyrite (e.g. $Cu(In,Ga)_3Se_5$) will probably appear [57]. The chemistry that occurs on the solid surface is a balance between the diffusion of the elemental (In,Ga) into the bulk and the formation of their selenides ($(In,Ga)_ySe$) on the surface followed by diffusion into the bulk. The latter process is complicated by the volatility of certain $(In,Ga)_ySe$. Roughly, vapor pressure and volatility decrease with an increase in Se content of the binary ($(In,Ga)_2Se \rightarrow (In,Ga)Se \rightarrow (In,Ga)_2Se_3$). Therefore, the net quantity of (In,Ga) incorporated into the solid is the difference between (In, Ga) and $(In,Ga)_ySe$ which are delivered/rejected and are a function of the local Se-vapor concentration and substrate temperature.

The (In,Ga) and Se incorporated into the solid system will require a reconstructing of the near-surface bulk into something that is consistent with an Cu-poor complex defect chemistry, i.e., Cu vacancy (V_{Cu}) and (In,Ga)-on-Cu ($(In,Ga)_{Cu}$) antisite defects. With sufficient (In,Ga) excess, the near-surface bulk will be characteristic of the $Cu(In,Ga)_3Se_5$ phases. However, the creation of defects adversely affects the cell performance and may be avoided by careful consideration of the mass transport kinetics described above. The process can be optimally designed to allow the incorporation of (In,Ga) and Se via reaction kinetics to form the chalcopyrite ($Cu_xSe_{(l)} \rightarrow Cu(In,Ga)Se_{2(s)}$), and disallow incorporation via diffusion kinetics to form defect-pairs in the defect-chalcopyrite.

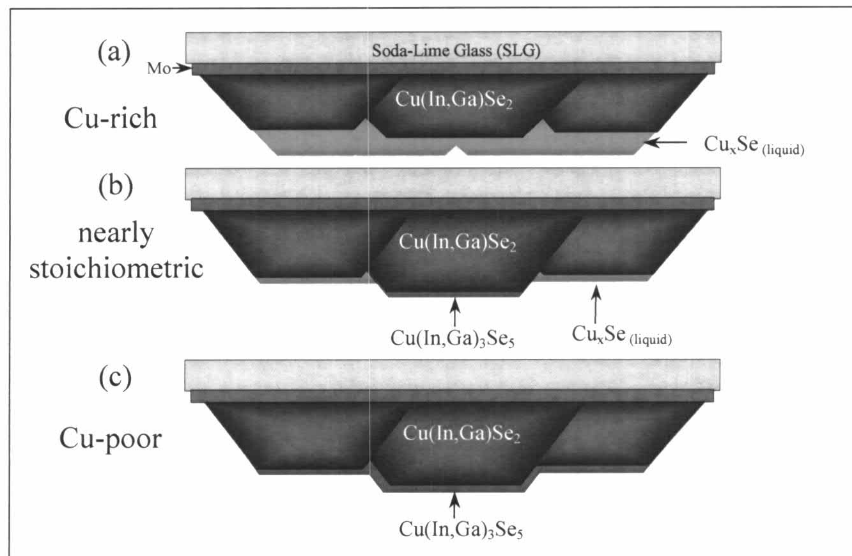

Figure 5.8: Pictorial representation of the Cu_xSe/surface modification process. (a) Cu-rich, (b) nearly stoichiometric, (c) Cu-poor [38].

The evolution of the bulk from Cu-rich to Cu-poor is pictorially shown in Fig. 5.8. The change in surface chemistry is also conductive to an end point detection (EPD) scheme that either observes a transition in surface composition

or state (liquid→solid) as presented in Section 5.1.1. Moreover, the evolution of the film thickness and growth mechanisms as a function of time are shown in Fig. 5.9.

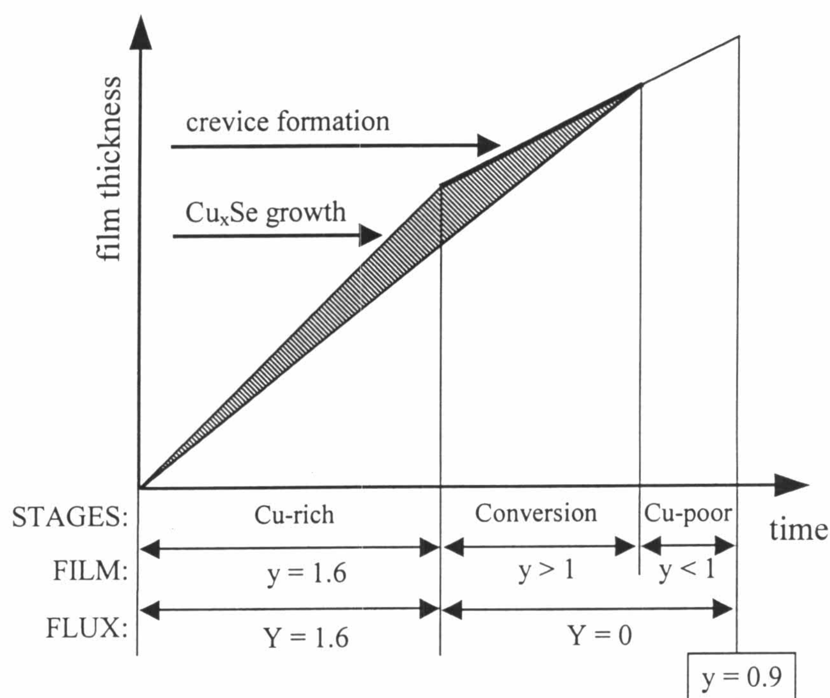

Figure 5.9: Growth model for the CURO process.

5.1.5 Cell Performances of the Films Grown by CURO Process

Using this end point detection as mentioned in Section 5.1.1, to control our CURO growth process, CIGS films were produced, and the standard device structure (Al/ZnO(Al)/CdS/CIGS/Mo/SLG) for the solar cells were fabricated as outlined in Section 4.1. The cell performance is then characterized using a standard current-voltage (I-V) measurement and a quantum efficiency (QE) measurement. The results of cell performances are plotted for a matrix of 2

rows, each row contains 8 cells and the total area of each cell is about 0.5x1.0 cm^2. A typical result of 16 cells on a 3x5 cm^2 substrate is shown in Fig. 5.10 and their statistical values are listed in Table 5.2.

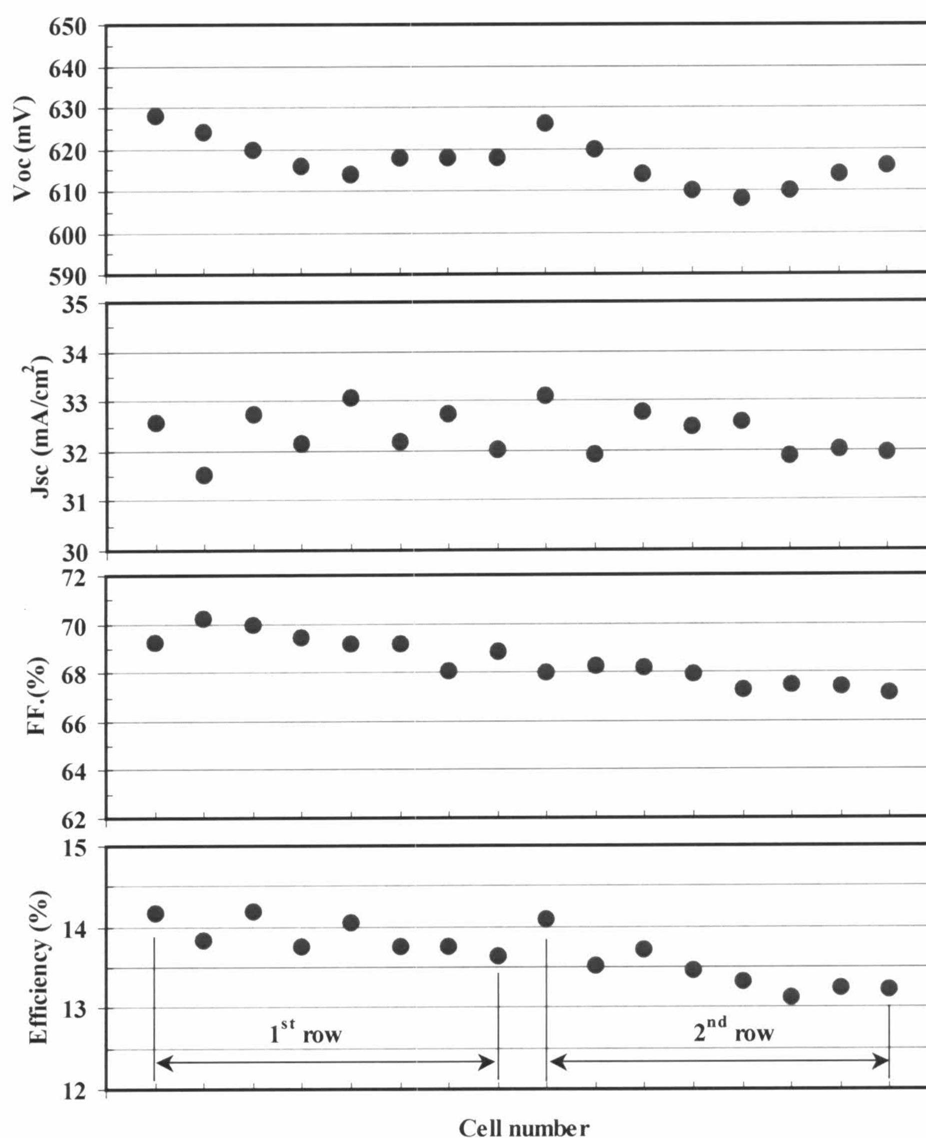

Figure 5.10: Typical cell performances, V_{oc}, J_{sc}, FF and efficiency for a sample grown by CURO process at $T_{sub} \approx 510^{o}C$, as a function of position, for a typical 3x5 cm^2 substrate. The sample is divided into 16 cells (2 rows and 8 columns) of 0.5 cm^2 each.

Table 5.2: Statistical values of the current-voltage parameters for the sample as shown in Fig. 5.10.

	V_{oc}(mV)	J_{sc}(mA/cm^2)	*FF*(%)	Efficiency(%)
Maximum	628	33.1	70.2	14.2
Minimum	608	31.5	67.2	13.1
Mean	617	32.4	68.5	13.7
S.D.	5.7	0.5	1.0	0.3

From a device point of view, the average efficiency of 14% show that the quality of CIGS film grown by our CURO process can be classified into the device-quality CIGS absorber layer. However, the cell parameters (V_{oc}, J_{sc} and *FF*) are not independent from each other and are controlled by the whole process of device fabrication. The trend of efficiency shows a level of uniformity of the CIGS film that is limited primarily by the experimental set-up. In most samples (over 1,000 cells), the level of uniformity is not found to be remarkably different for depositions grown at the other substrate temperatures, deposition times and the contents of Cu in the Cu-rich stage. Therefore, the distribution of the cell parameters is limited mainly by the homogeneity of CIGS film that is effected directly by the configuration of the CIGS deposition system (e.g. the background pressure and the distance from the four sources to the substrate).

5.1.6 Conclusions: CURO Process

The *in situ* monitoring of T_{pyro}, T_{sub} and OP in the deposition of CIGS absorber layer film was developed to detect the desired Cu-deficient composition ($y \approx 0.9$) of the two-stage growth or CURO process. The high quality CIGS film using this monitoring technique can be fabricated to give the high performance solar cells on the 5x6 cm^2 substrate. We achieved the best cell with efficiency 14.2% (V_{oc} = 620 mV, J_{sc} = 32.7 mA/cm^2, FF = 70.0 %, without AR), where both I-V and QE characteristics are presented in Fig. 5.11 and 5.12, respectively. Finally, these *in situ* monitoring can be modified to be used in the large area for mini-module and module fabrication.

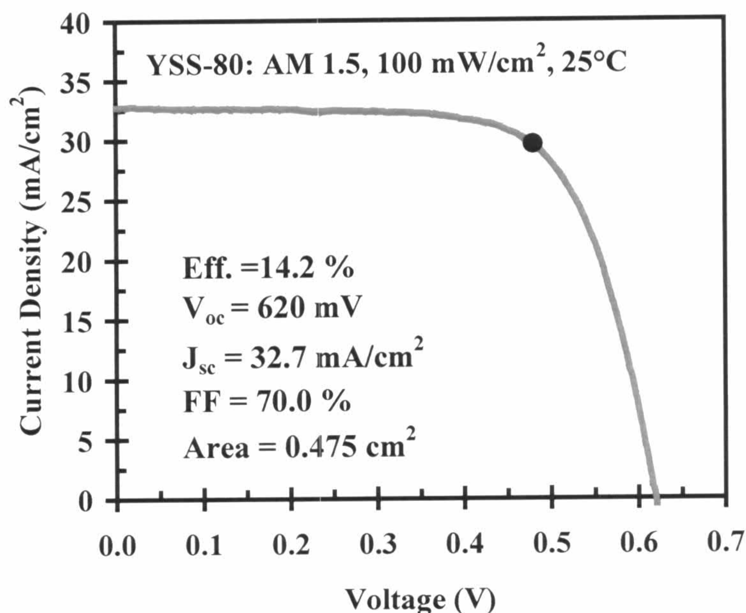

Figure 5.11: I-V curve of the best CIGS solar cell using the *in situ* monitoring in the typical two-stage or CURO process at $T_{sub} \approx 510^{o}C$.

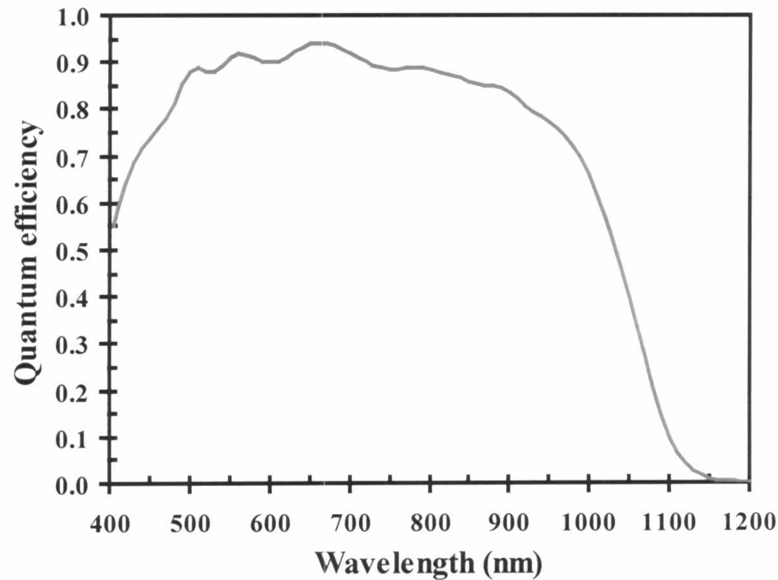

Figure 5.12: QE of the best CIGS solar cell using the *in situ* monitoring in the typical two-stage or CURO process at $T_{sub} \approx 510^{o}C$ as shown in Fig. 5.11.

5.2 Results and Discussion of the CIGS Films Grown by CUPRO Process and Cell Performances

5.2.1 Film Growth by CUPRO Process

The growth of CIGS films by modified two-stage or CUPRO process as previously discussed in Section 4.2, we show typical temperature profiles of three metal sources (Fig. 5.13(a)), the heating output power for regulating the substrate at a constant temperature of 500°C (Fig. 5.13(b)) and the values of Cu content of the growing film (Fig. 5.13(c)). Various characteristic durations are defined in Fig. 5.13(a) and 5.13(b), in three different ways relative to the source control ($t_1 = t_{1a}+t_{1b}+t_{1c}$ and t_2), the flux composition ($Y < 1$ or $Y > 1$ or $Y = 0$) or the film composition ($y < 1$ or $y > 1$).

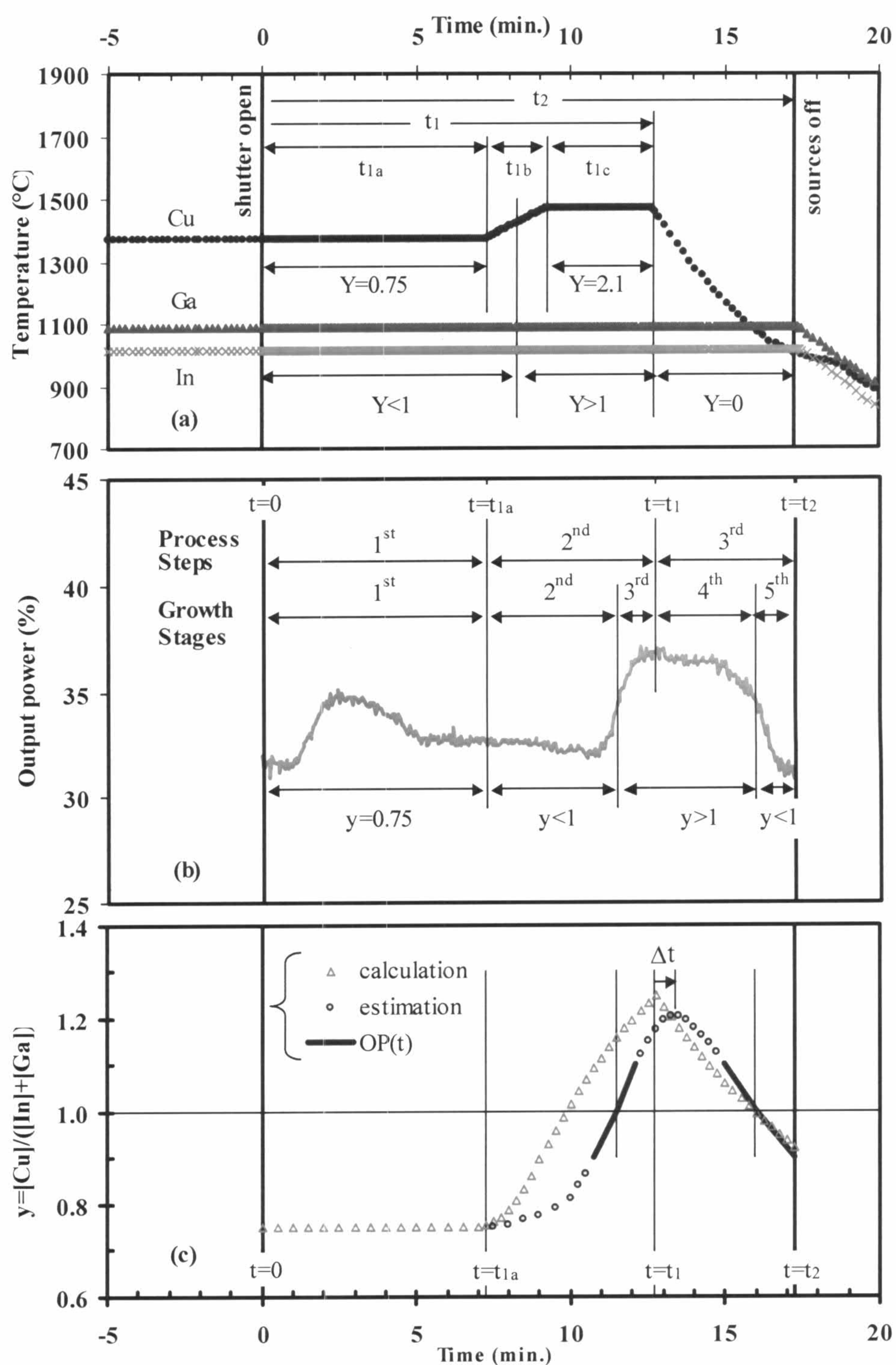

Figure 5.13: (a) Typical temperature profiles of Cu, In and Ga sources by CUPRO process. (b) The *in situ* monitoring of output power signal of the deposition process. (c) The values of Cu content of the growing film from both calculation and estimation.

During the process as shown in Fig. 5.13(a), the temperatures of the substrate and Se source were fixed at 500°C and 315°C, respectively. The temperatures for other sources were chosen so that the total acquired film thickness was between 2 and 2.2 μm, for total deposition time less than 20 min. Using the $T_i = f(\Phi_i)$ relationships, the temperatures of the metal sources are calculated so that x is constant throughout the whole process (here $x \approx 0.25$) and so that during the time t_{1a} the flux (Y) and film (y) compositions are equal to 0.75. The Cu source temperature is then increased over the time t_{1b} so that the global flux changes from Cu-poor (Y<1) to Cu-rich (Y>1) conditions where it is maintained during the time t_{1c} until the film becomes sufficiently Cu-rich ($y > 1.1$). At this point (t_1) the Cu source is turned off, the Cu flux rapidly falls to zero and, as in the CURO process, the film returns to Cu-poor composition. Finally, the film is interrupted when $y \approx 0.9$. The triangles in Fig. 5.13(c) are calculated from the source temperatures in Fig. 5.13(a) under the hypothesis that the source dynamics is negligible (i.e. that the $T_{Cu} = f(\Phi_{Cu})$ relationship is continuously valid). Especially during t_{1b} this is not true as the dynamic situation of the source leads to a delay between the temperatures measured by the thermocouple and those of the evaporating surface.

The *in situ* monitoring of output power signal during the deposition process is shown in Fig. 5.13(b). This signal shows typical variation of the output power (OP) of the temperature controller which keeps the substrate at a constant temperature. As in the CURO process we have analyzed that the transition in the OP signal occurs for variations of $y(t)$ between 1.1 and 0.9. Therefore, this signal is used to position the points where $y(t) = 0.9$ and

$y(t)$ = 1.1, between which the solid lines in Fig. 5.13(c) are determined from the expected evolution of the integral film composition.

The circles represent an estimation of the evolution of $y(t)$ outside of the values "visualized" by the OP signal, taking into account the dynamics of the Cu source, both on the t_{1b} up-heating and on the non-instantaneous turn-off at t_1. This leads to a delay, as shown in Fig. 5.13(c), of the point in time where the maximum value of y is reached. This maximum y value is not obtained at t_1 but at $t_1+\Delta t$. In the present example the end of the growth (i.e. t_2: the point in time where $y \approx 0.9$) as determined by the calculated values of y or as determined by the OP signal are not greatly different. Nevertheless, in practice, it is found that the use of the OP signal to target the final composition $y(t_2)$ of the film is much more reliable. This OP signal also used to determine the time t_1 at which the power of the Cu source is turned off, by estimating the time where $y(t) \geq 1.1$.

5.2.2 Effect on Film Orientation: (112) vs. (220)(204)

Six $Cu(In,Ga)Se_2$ films (A, B, C, D, E, and F) were grown by various recipes depicted in Fig. 5.14. All of these samples were grown at the substrate temperature of 500°C. Films A and B are grown as uniform flux references, respectively at y = 0.90 (the targeted terminal composition) and y = 0.75 (the chosen initial Cu-poor value used in the present CUPRO process). Films C and D are uncompleted layers, whereas film E is the result of a completed CUPRO process. Film C represents the state of the growing film just prior to the increase in Cu-flux, whereas film D is the state just prior to the film becoming

globally Cu-rich. Film F is given as reference to the CURO process, where the initial growth is only moderately Cu-rich (i.e., when $y \approx 1.1$).

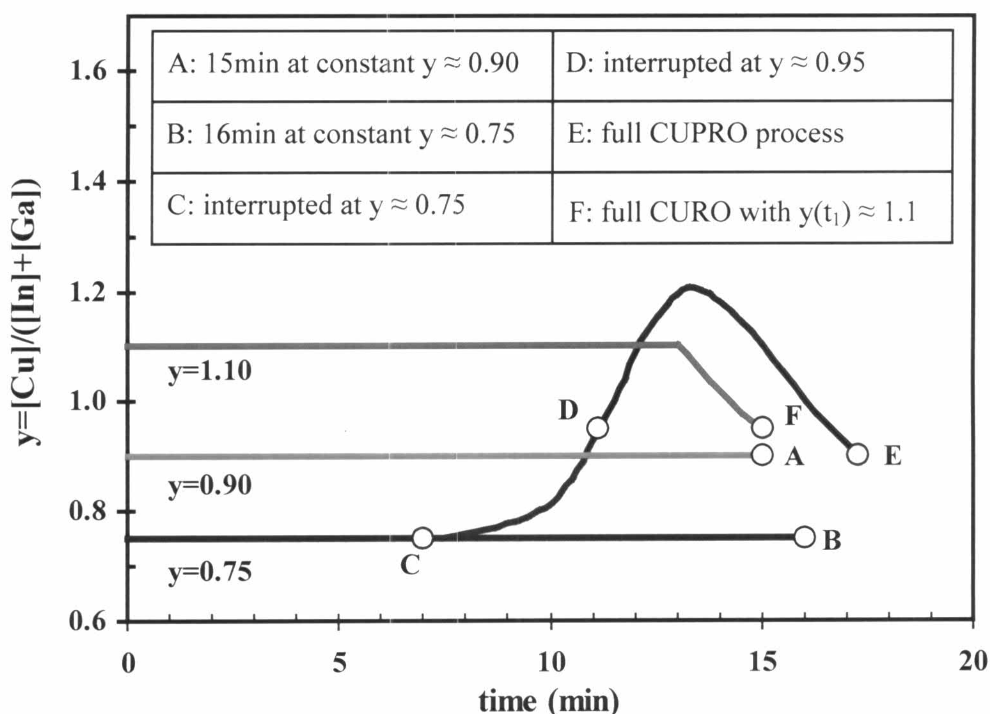

Figure 5.14: Six different film growths (A-F) produced from the different *y(t)* evolutions.

XRD measurements are made, and in particular the (112), (220)(204) and (116)(312) peaks are shown in Fig. 5.15. Although the plotted XRD spectra contains more information than the peak intensities, we here limit our use of this data to measuring the z = I(112)/I(220)(204) ratios, given in Table 5.3.

In comparing the results for the films A and B, it is seen that these Cu-poor uniform films are (220)(204) oriented to a degree that increases with the decreasing y value. The evolution of the film grown during the CUPRO process can be studied by the comparison of films C, D, and E. However, the measured differences between the z ratios for these films are not considered

significant, as they are within the reproducibility of each experiment. The orientations of films C, D, and E are all considered to be comparable to that of film A. On the other hand, the difference between these z ratios and that of film B is considered representative. In particular, in comparing films B and C it is seen that by growing a thicker $y = 0.75$ film, there is an increase in the extent of the (220)(204) orientation. This will be complemented by SEM/TEM cross-sections given hereafter in Section 5.2.3.

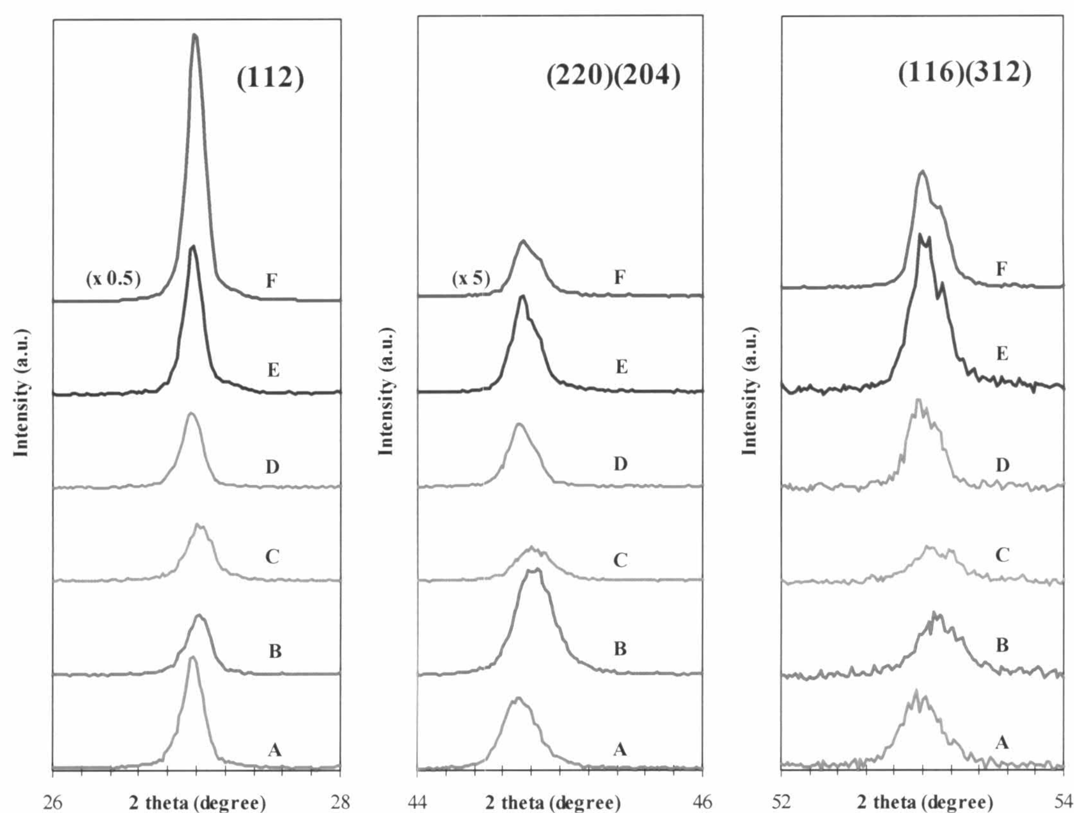

Figure 5.15: Evolution of the selective XRD results from (112), (220)(204) and (116)(312) peaks for the films shown in Fig. 5.14.

Although the films A, E, and F all have approximately the same terminal composition ($y \approx 0.90$), films A and E have a similar degree of (220)(204) orientation ($z \approx 1.5$), whereas film F is highly (112) oriented with $z \approx 50$. The

comparison between films A and F demonstrates the impact on the crystal orientation of a Cu-rich versus a Cu-poor initial film growth. As the Cu-$K_{\alpha 1}$ and Cu-$K_{\alpha 2}$ radiation was used as incident radiation. The (116)(312) peak splitting is more clearly resolved for the films E and F using Cu-rich state which have higher crystalline quality. Also, as will be shown later in Section 5.2.3, the similar z ratios of films A and E are not indicative of similar morphology; these two films differ considerably from this point of view.

Table 5.3: Orientation ratios z = I(112)/I(220)(204) for the films shown in Fig. 5.15.

Film	z = I(112)/(220)(204)
A	1.6
B	0.6
C	1.7
D	1.2
E	1.5
F	49.2

Although the CUPRO process used here can also be considered as being comprised of three deposition process steps (Cu-poor, Cu-rich, Cu-off), it is not the "three-stage" process as defined by others [42, 58, 59]. Nevertheless, it is interesting to compare the proposed criteria for (220)(204) preferred orientation. According to Chaisitsak *et al.* [42] the factor dictating the orientation is the $\Phi_{Se}/(\Phi_{In}+\Phi_{Ga})$, ratio during the first stage, which is Cu-free in the "three-stage" process. It is shown that (220) orientation results from high Se

overpressures (i.e., $\Phi_{Se}/(\Phi_{In}+\Phi_{Ga}) > 7.6$). While, according to Contreras *et al.* [58] the Mo/SLG substrate, its Na content, and its temperature during the second stage are shown to result in control of the preferred orientation. In our experiments, the Se overpressure is low-$\Phi_{Se}/(\Phi_{Cu}+\Phi_{In}+\Phi_{Ga})$ is estimated to be of the order of 2 during the Cu-poor growth, and of the order of only 1.2 in the Cu-rich growth, and the Mo layer is baseline quality (i.e., not particularly impermeable to the Na). However, our experiments do corroborate with Contreras *et al.* [58] in that a Cu-rich growth hinders the attainment of the (220)(204) orientation. This would explain why film F, which has been grown in Cu-rich conditions, is (112) oriented.

5.2.3 Effect on Film Morphology

SEM is used to examine the morphology of the different films presented in Fig. 5.14. A first comparison is made between the two films A (y=0.90) and B (y=0.75) grown under uniform flux conditions. Shown in Fig. 5.16, the cross-sections of these two films present very a similar morphology, but show film B to be a little thicker than film A. This thickness difference is explained by a combination of the two following facts: (a) the deposition time of film B is 1 min longer than that of film A; (b) both films are grown under the same Cu flux, but both the In and Ga fluxes are higher for the growth of film B. Both films exhibit a small grain structure near the Mo back contact, while the grain size increases towards the front surface of the films. Also shown in Fig. 5.16 are the intermediate uncompleted layers (C and D) as well as the final result (E) of the CUPRO growth process presented in Fig. 5.14. Film C is produced under the same growth conditions as film B, except that the growth is interrupted at 7

rather than 16 min. Comparing the SEM cross-sections of these film C and B, it can be seen that a more "textured" overgrowth becomes dominant as the thickness increases. It would be consistent with the XRD data to interpret this "textured" over layer as being increased in the (220)(204) orientation. Film D is the evolution of film C resulting from the increase of Cu vapor in flux, but, as previously stated, prior to the moment where the global composition of the film becomes Cu-rich.

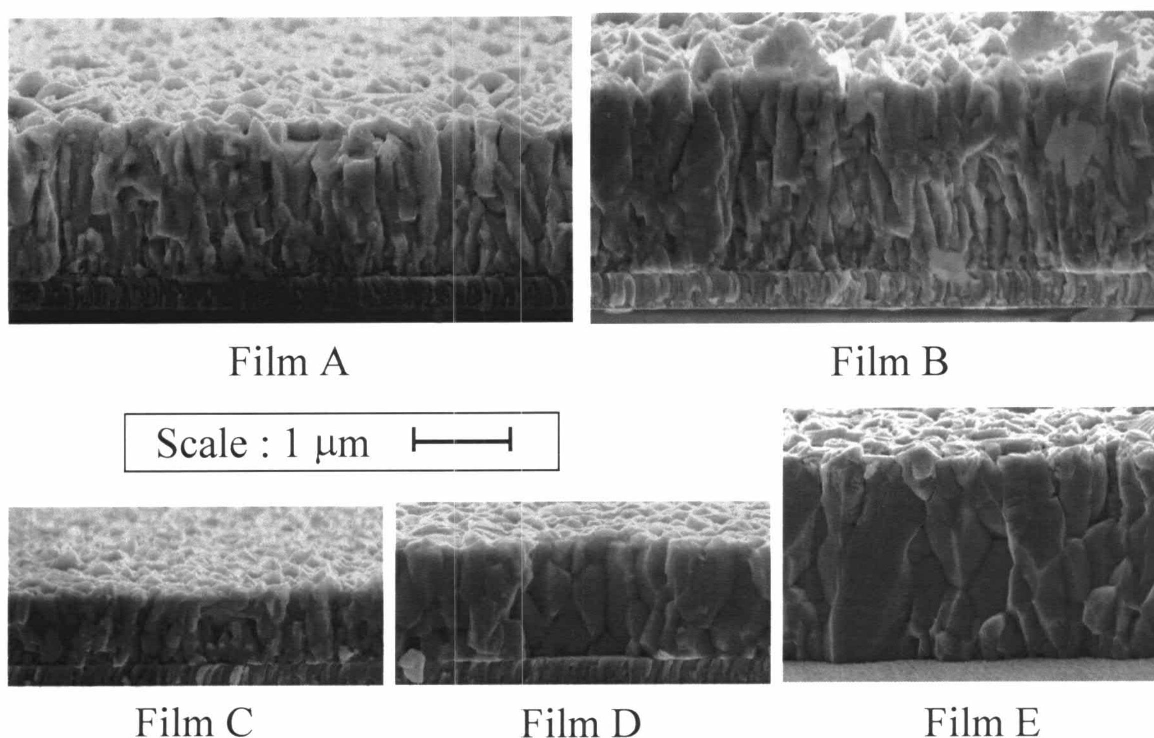

Figure 5.16: SEM micrographs (cross-section about 10° tilt) of the films shown in Fig. 5.14 (except film F). Top row: films A and B, uniform fluxes at $y = 0.90$ and $y = 0.75$. Bottom row: films C-E, evolution of the CUPRO growth.

It is most remarkable that the grain size of film D appears larger, even at the rear of the film, than does that of film C. We believe that recrystallization occurs as a result of the change in the metal flux ratios. Examination of a slightly later point in this growth, when the global film composition has exceeded y=1 (film not shown in Fig. 5.14, 5.15 or 5.16), does not result in any significant difference relative to film D. The morphology of film E, at the end of the CUPRO process, appears to be very similar to that of film D, except that the total thickness is then of the order of 2 μm and that crevices are observed in the top fraction of the film that has been added in the evolution from D to E.

For increased clarity, the films shown in Fig. 5.16 (except film A) are further examined by TEM cross-sections. These are shown in Fig. 5.17 and support what has been already seen in the SEM study. In particular, the evolution from film C to film D clearly permits the justification of the term "recrystallization". These TEM images also make very evident the morphological differences between the films grown by the CUPRO process versus those grown at constant flux. As for the SEM, it can also be seen that the evolution from film D to film E, apart from the additional thickness, is mostly in the formation of crevices seen in this additional material. At this point one could question whether film D is of device quality or not, possibly by producing a film in a similar manner, but at a device-relevant thickness (e.g., at least > 1.5 μm). The questions are: why drive the film Cu-rich only to bring it back to $y \approx 0.9$ if this only results in the creviced surface; and does the globally Cu-rich growth (growth stages 3 and 4 in Fig. 5.13(b), where there is existence of Cu_xSe) do anything special relative to the final film quality? In the present work, one of the reasons for the complete CUPRO scheme is to enable easy use

of the EPD. Although the stopping point required to produce film D is within the zone where the OP signal evolves, it is considerably more critical to use as an EPD than is the Cu-rich to Cu-poor transition.

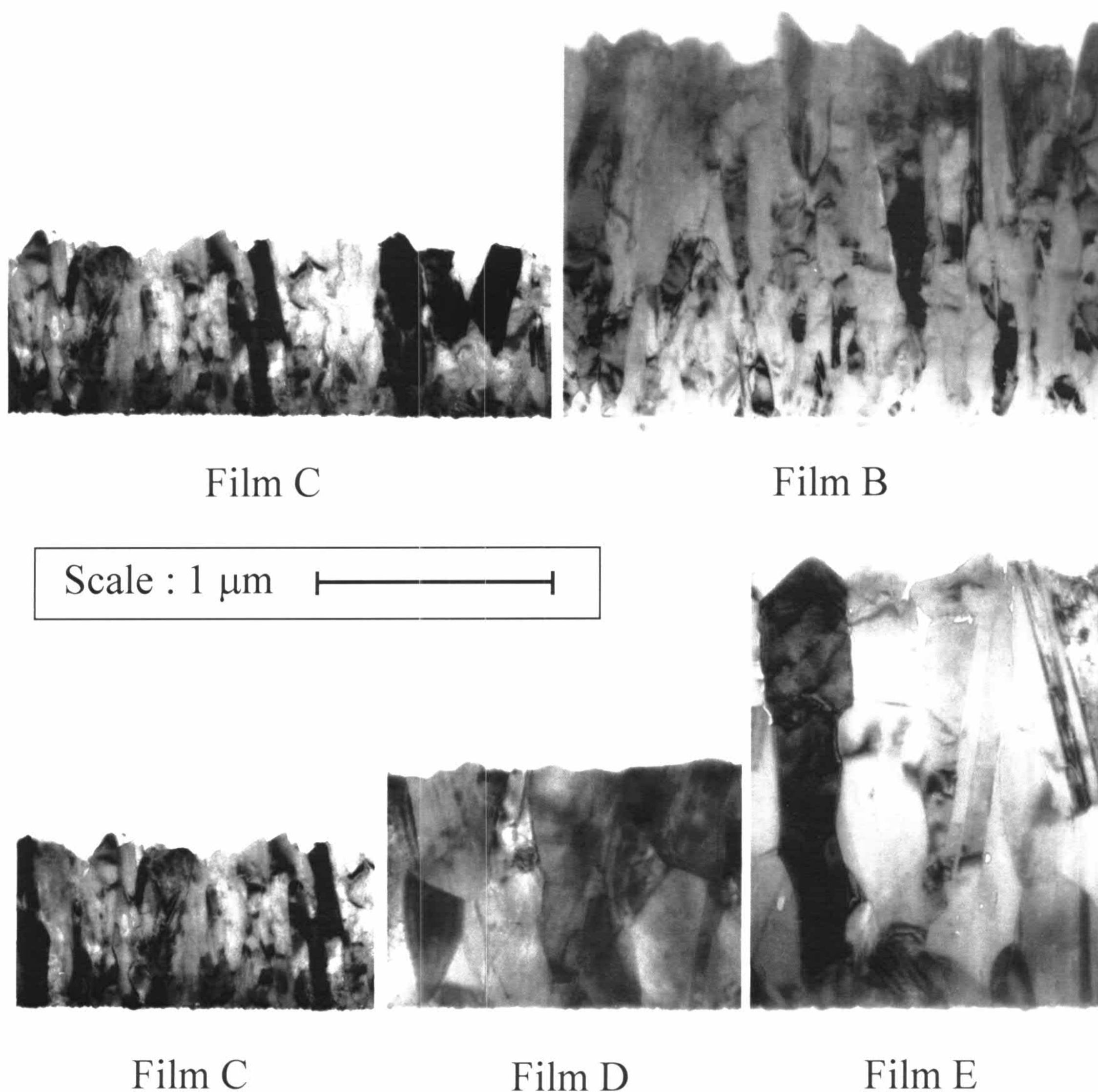

Figure 5.17: TEM micrographs (cross-section) of the films shown in Fig. 5.14 (except film A and film F). Top row: films C to B, evolution of the uniform flux growth at y = 0.75. Bottom row: films C-E, evolution of the CUPRO growth.

5.2.4 Effect on Substrate Temperatures

To study the effect of substrate temperatures on the property of film grown by CUPRO process, four $Cu(In,Ga)Se_2$ films are produced by the CUPRO process at the four substrate temperatures of 475, 500, 525 and 550°C. The growth times are between 15 and 20 min. For all of these films, the first stage Cu-poor growth is performed at a film composition of y = 0.75 and the Cu-rich stage achieves approximately $y \approx 1.2$ before the Cu-off stage where the film composition evolves back to $y \approx 0.9$. The typical evolution of $y(t)$ is similar to that of film E as previously shown in Figure 5.14. To examine the crystalline status of the films, XRD measurements are made, and in particular the (112), (220)(204), and (116)(312) peaks are shown in Fig. 5.18.

Three substrate temperature dependent trends are observed. Firstly, it can be seen that for the higher temperatures the film orientation as measured by the values of I(112)/I(220)(204) ratio (Table 5.4) is increased from weakly (112) to weakly (220) orientation. Secondly, there is a shift of the peak positions towards lower angles with increasing substrate temperatures. Thirdly, the (220)(204) and the (116)(312) peak splitting is more clearly resolved for the higher temperatures. It can therefore be concluded that at the higher substrate temperatures, the films are more (112) oriented, have higher crystalline quality, and contains less Ga, and this despite the identical set temperatures for the In and Ga sources.

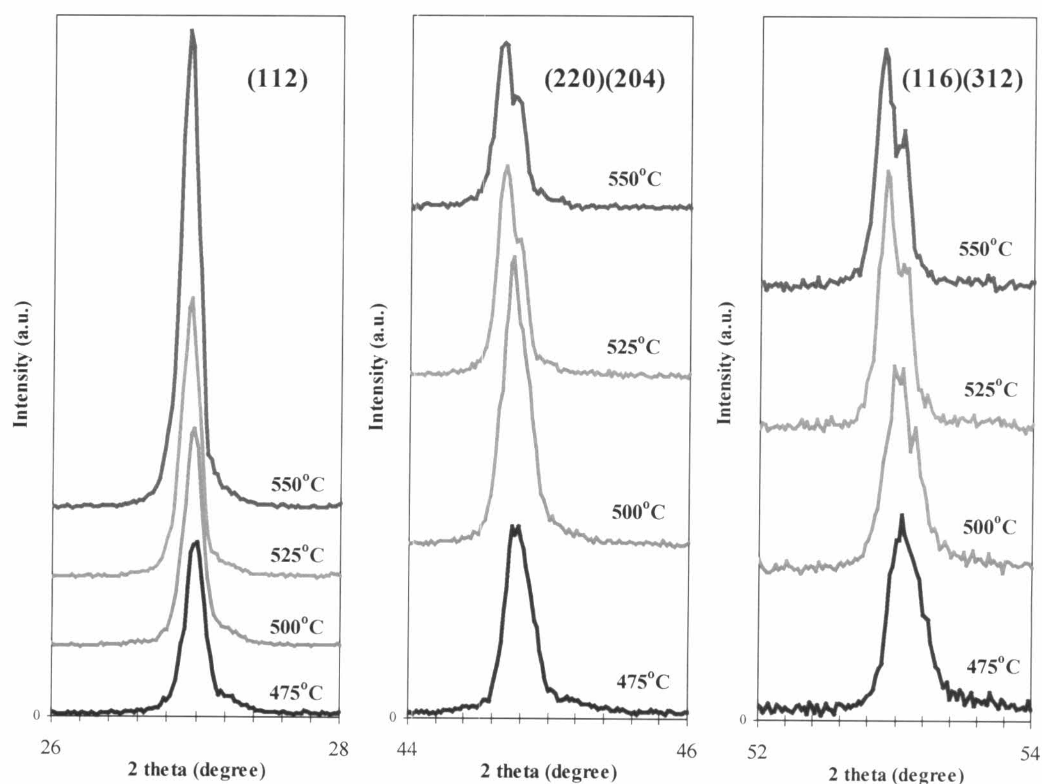

Figure 5.18: Evolution of the selective XRD results from (112), (220)(204) and (116)(312) peaks for the films grown at different substrate temperatures.

Table 5.4: Orientation ratios z = I(112)/I(220)(204) for the films grown at different substrate temperatures.

T_{sub} (°C)	z = I(112)/I(220)(204)
475	1.9
500	1.5
525	2.8
550	5.9

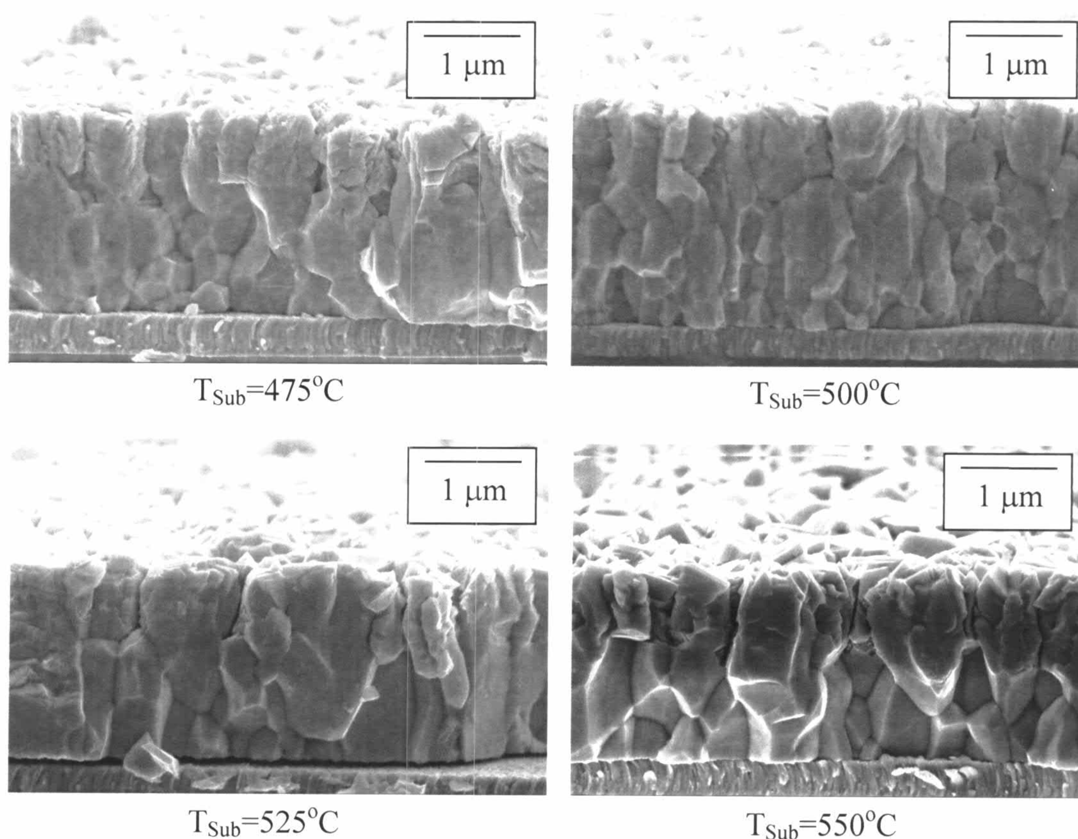

Figure 5.19: SEM micrographs (cross-section about 10° tilt) of the four CUPRO grown $Cu(In,Ga)Se_2$ films at different substrate temperatures of 475, 500, 525, and 550 °C.

Figure 5.19 shows SEM cross-sections of the four films here considered. The first observation is that the bottom two thirds of the films are similar for all substrate temperatures whereas some differences are observed between the top thirds of the films. For the bottom fractions, the obtained grain size is relatively large and the film is dense, and this even when the substrate temperature is 475°C. On the other hand, a rougher top structure is observed for the lower temperatures while sharper and larger crystalline edges are found at the higher temperatures. Also, and particularly clearly for the highest temperature, the top fractions of the films exhibit crevices, as has already been shown by means of

polished cross-sectional SEM studies in Ref. [53]. It must be remarked that the thickness of the film deposited prior to the beginning of the Cu-rich growth is approximately that of the bottom two thirds of the films. It would thus appears that the initial Cu-poor growth does not seem to result in an obvious temperature dependence, whereas the Cu-rich part of the growth differs for the different substrate temperatures. This is not unreasonable considering that the Cu-rich growth is reported to occur in the presence of secondary phase segregation of Cu_xSe, and that this Cu_xSe has a solid-liquid phase transition within the explored temperature range. The improved crystallinity of the growth corresponds to the temperatures where the Cu_xSe is liquid and can act as a flux for the growth [39]. Nevertheless, possible small variations such as the exact terminal composition of the films could also play a role in the morphological differences, especially those of the surface region, observed in these SEM cross-sections.

5.2.5 Cell Performances of the Films Grown by CUPRO Process

Using the end point detection via OP to control a Cu-Poor-Rich-Poor sequence in the CUPRO growth process, CIGS films were produced, where a standard device structure (Al/ZnO(Al)/CdS/CIGS/Mo/SLG) for the solar cells were also fabricated (using the baseline process of Ångstrom Solar Center, Uppsala University) as outlined similarly in Section 4.1. Cell performances for a sample grown by CUPRO process at $T_{sub} \approx 500^{\circ}C$ are plotted for a matrix of 4 rows and 8 columns where the total area of each cell is about 0.5x1.0 cm^2. A

typical result of 32 cells on a 5x5 cm^2 substrate is shown in Fig. 5.20 and their statistical values are listed in Table 5.5.

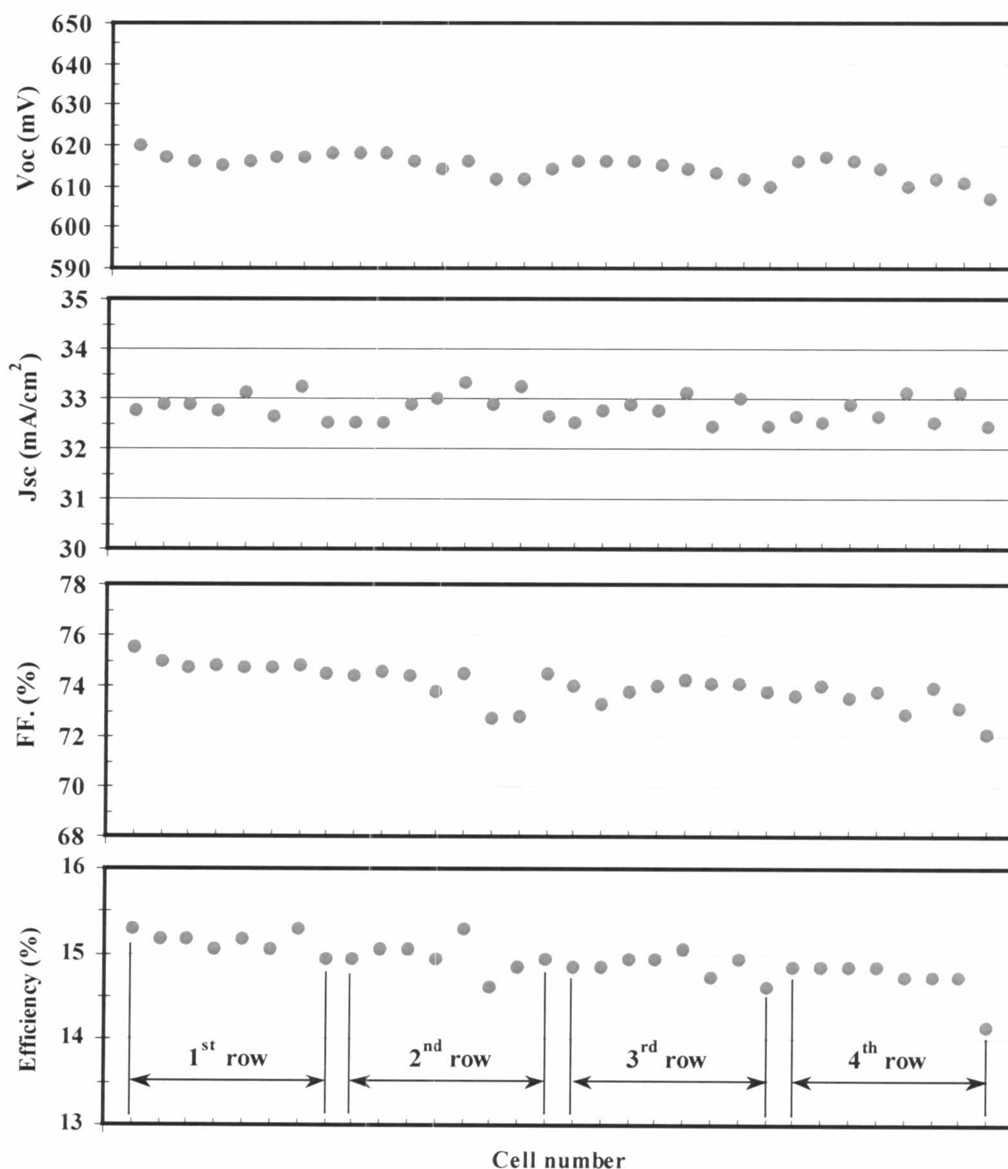

Figure 5.20: Typical cell performances for a sample grown by CUPRO process at $T_{sub} \approx 500^oC$, as a function of position, for a typical 5x5 cm^2 substrate. The sample is divided into 32 cells (4 rows of 8 columns) of 0.5 cm^2 each.

Table 5.5: Statistical values of the current-voltage parameters for the sample as shown in Fig. 5.20.

	V_{oc}(mV)	J_{sc}(mA/cm^2)	FF(%)	Efficiency(%)
Maximum	620	33.3	75.5	15.3
Minimum	607	32.4	72.1	14.2
Mean	615	32.8	74.0	14.9
S.D.	2.8	0.3	0.7	0.2

In Table 5.5, the average efficiency of 15% shows a superior device-quality of CIGS film grown by CUPRO process, where the fill factor is observed to be a primarily parameter in improving cell performances. As plotted in Fig. 5.20, the trend of efficiency indicates the same level of uniformity with respect to that of CURO process (Fig. 5.10). However, a small variation of V_{oc} (within 10mV) are also observed which could be due to a small gradient of [Ga]/([In]+[Ga]). In most samples (over 2,000 cells), the level of uniformity (as shown in Fig. 5.20) is not found to be remarkably different for depositions grown at the other substrate temperatures and deposition times. Some of the samples have shown less variation of cell parameters than that in Fig. 5.20, and almost all cells have the efficiency levels between 14-15%.

Confirmation of the evolution of the Ga content is found in the behavior of the devices produced from the CIGS films with the different substrate temperatures (475, 500, 525 and 550°C). The cell performances of the best cells for their substrate temperatures are shown in Table 5.6.

Table 5.6: Cell performances of the best cells grown by CUPRO process for the four studied substrate temperatures.

T_{sub}(°C)	V_{oc}(mV)	J_{sc}(mA/cm^2)	*FF*(%)	Efficiency(%)
475	617	33.7	73.7	15.4
500	618	34.0	75.5	15.9
525	592	35.5	74.8	15.7
550	580	35.5	72.9	15.1

In Fig. 5.21 and 5.22, there is a clear shift of approximately 50 nm in the QE cut-off values as well as a trade-off between J_{sc} and V_{oc} in the I-V characteristics compatible with a Ga content change in the order of about 10% (i.e. 25 % $\leq$ [Ga]/([In]+[Ga]) $\leq$ 35 %). If we neglect the thermal interactions between the substrate and the sources (believed to be only the second order effect), then the above indicates a lesser sticking coefficient of the Ga versus the In for the higher substrate temperatures. As to whether loss occurs during the Cu-poor or during the Cu-rich stages of the growth, a more detailed study is needed and is not included in this work.

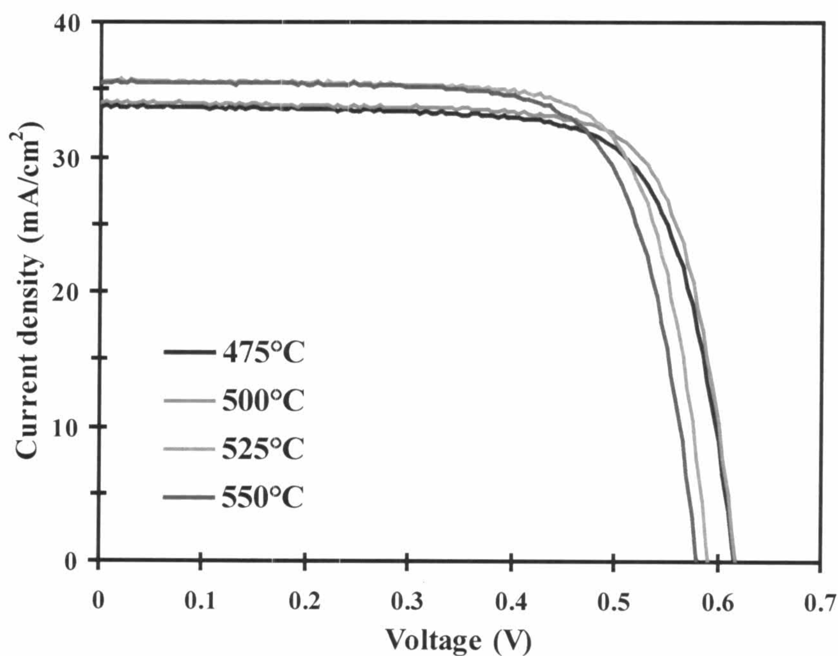

Figure 5.21: Current-voltage characteristics of the best cells grown by CUPRO process for the four studied substrate temperatures.

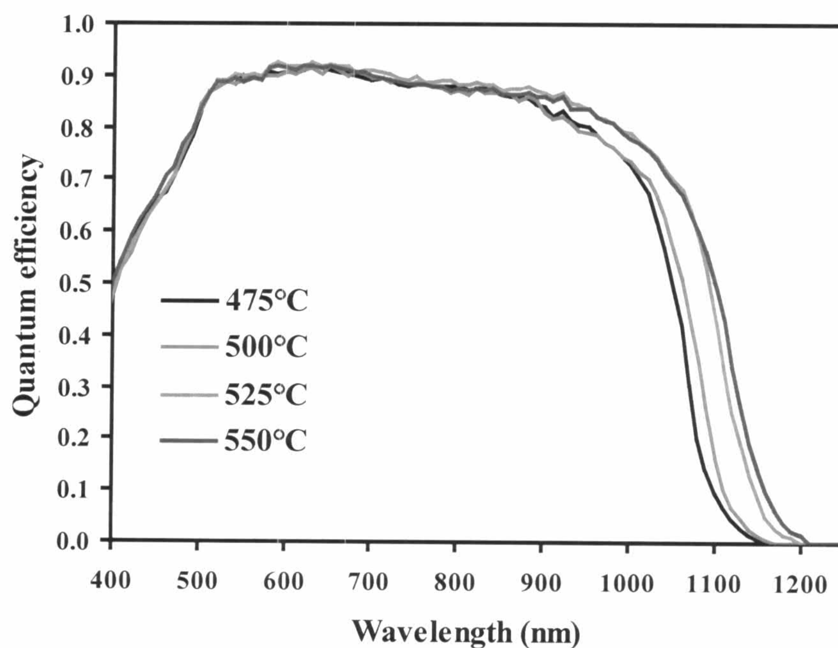

Figure 5.22: Quantum efficiencies of the best cells grown by CUPRO process for the four studied substrate temperatures shown in Fig. 5.21.

5.2.6 Five-Stage Growth Model

The present primitive growth model attempts to explain these results. The pretensions of this model are modest and are not more than a "probable picture". The objective is to understand the "base" recipe, considered to correspond to $T_{sub} = 500$ °C. Although the control of the CUPRO process occurs in three steps of the Cu flux ($\Phi_{Cu} = \text{low}$, $\Phi_{Cu} = \text{high}$, $\Phi_{Cu} = 0$) or (constant y, increasing y, decreasing y) represented in Fig. 5.13(b), we further subdivide, distinguishing $y < 1$ from $y > 1$, and examine the film growth in five stages, also represented in Fig. 5.13(b) as well as Fig. 5.23.

During the first stage of the growth, where both y and Y are fixed at 0.75, a compositionally uniform film is grown, initially exhibiting small and close to randomly oriented crystallites. As the film grows thicker, the (220)(204) oriented grain growth dominates (probably due to a more rapid growth than that of the (112) orientation), and the film becomes increasingly (220)(204) oriented. We believe that the chosen value of y is not critical, and it is observed that films grown uniformly at $y = 0.90$ behave in the same way as those grown at $y = 0.75$, i.e. film A and film B are very similar.

During the second stage of the growth, where the global composition evolves from $y = 0.75$ to $y = 1$, the top surface of the film is grown more Cu-rich than is the bulk, and we believe that this Cu gradient results in a Cu diffusion that acts as a driving force for the recrystallization of the film. This recrystallization occurs without much reorientation as the (220)(204) preferred orientation is maintained (film C versus film D). Even assuming that Cu_xSe could be locally present at the growing surface, one argument against the

postulate the importance of a liquid state (cf. solid-liquid-vapor (SLV) growth [39]) of this Cu_xSe in this second stage is that in Section 5.2.4. We have not observed the recrystallization to be dependent on the substrate temperatures, for growths at 475, 500, 525 and 550°C (i.e., for temperatures above and below the solid-liquid transition for Cu_xSe at 523°C). Moreover, if Cu_xSe had been present, we believe that it would have affected the OP signal, but this was not observed. At the end of this second stage, and assuming very rapid Cu diffusion, the film is single-phase (to the detection limit of the XRD, analysis not shown), large-grain (Fig. 5.16 and 5.17), weakly (220)(204) oriented ($z \approx 1.5$, Table 5.3), and believed to be uniform and stoichiometric $Cu(In,Ga)Se_2$. The hypothesis of very rapid Cu diffusion is supported by the previously staged fact that the OP signal is indicative of a Cu-poor surface, i.e. a surface without Cu_xSe segregation, throughout this second stage of the growth. In the latter part of this second stage, the Cu flux is very high ($Y > 2$), and if the Cu diffusion is not at least as fast as the excess Cu accumulation at the surface (relative to $Cu(In,Ga)Se_2$ stoichiometry), segregation of Cu_xSe at the surface would be expected.

The third stage of the growth is increasingly Cu-rich from $y = 1$ until the maximum value of y, where the Cu source is turned off (neglecting the source dynamics). Here, an overgrowth on the previous stoichiometric $Cu(In,Ga)Se_2$ layer occurs, consisting of the expected two-phase system of additional stoichiometric $Cu(In,Ga)Se_2$ with an increasing fraction of Cu_xSe as a secondary phase, as discussed in Section 5.1. In this overgrowth, the Cu_xSe segregates into grain boundaries of the additional $Cu(In,Ga)Se_2$ (generated in this third stage), but without going down into the previous layer. This is mainly

supported by the fact that the crevice depth is found to be limited to the material deposited after the end of the second stage.

The fourth growth stage is defined from the moment when the Cu source is turned off until the moment the film again becomes globally stoichiometric for the second time. This is the stage where the secondary Cu_xSe phase is consumed by its reaction with the incoming fluxes of In, Ga and Se and converted into $Cu(In,Ga)Se_2$. At this stage, migration must occur, as the vapor distribution is uniform whereas the Cu_xSe is not. This migration is thought to result in the crevice formation observed in these films. This is supported by the fact that the depths of the crevices are limited to the fractional thickness of the films grown under the Cu-rich conditions, and that the Cu_xSe segregation is believed to be in the grain boundaries. Therefore, it is hypothesized that the crevices are formed where the Cu_xSe segregated in the third stage.

Further support is found in the fact that films grown by the CURO process as discussed in Section 5.1, such as film F in Fig. 5.14, for which there is no initial Cu-poor growth and thus no stoichiometric undergrowth, exhibit crevices that can be as deep as the total film thickness, extending down to the rear Mo contact. In addition, it has been found (although not shown here) that films grown by the CUPRO process using different extents of the Cu excess (i.e. different times t_{1c} in Fig. 5.13(a)) show different average crevice depths. At the end of this fourth stage, the film is globally stoichiometric, but the layer has undergone three distinct mechanisms resulting in stoichiometric $Cu(In,Ga)Se_2$. The first was the under layer and crevice-free material recrystallized by the action of the second stage, the second was the $Cu(In,Ga)Se_2$ grown in equilibrium with the Cu_xSe during the third stage, and

the third was the $Cu(In,Ga)Se_2$ resulting from the reaction of the Cu_xSe with the In, Ga and Se vapor in this fourth stage.

In the fifth and final stage of the growth, by the continuing fluxes of In, Ga and Se, the film is driven back to sufficiently Cu-poor conditions, so as to result in quality device material. The terminal value of $y = 0.90$ is controlled by the use of the End Point Detection (EPD) method. Here, we satisfy ourselves with the ability to accurately control the terminal global composition (at least as far as the y value is concerned) and with the ability to result in quality devices.

A "pictorial history" of the above model is attempted in Fig. 5.23. This figure represents the evolution of the film depth and growth mechanisms as a function of time and should be examined in relation to Fig. 5.13.

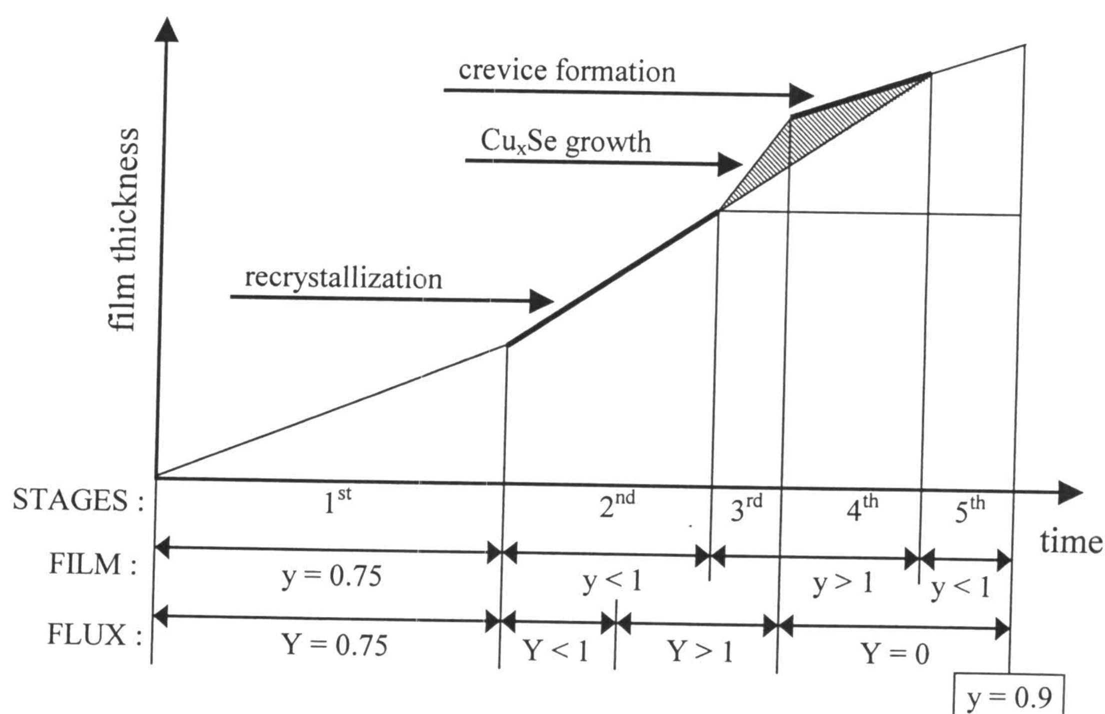

Figure 5.23: Five-stage growth model.

5.2.7 Conclusions: CUPRO Process

The CUPRO process has interesting qualities for practical producibility. It can be monitored by the simple end point detection (EPD) method, it uses moderate and constant substrate temperatures, the only deposition variable is the Cu flux, and rapid growth is shown to result in uniform $Cu(In,Ga)Se_2$ films for quality devices. The control of the process can be considered in three steps (low Cu flux, high Cu flux, no Cu flux) whereas the film growth is considered in five stages. The first is the growth of a Cu-poor and weakly (220)(204) oriented small grain layer, the second is recrystallization by Cu-diffusion until stoichiometry, the third is overgrowth of the bi-phase system $Cu(In,Ga)Se_2 + Cu_xSe$, the fourth is consumption of the secondary Cu_xSe phase, and the fifth is attainment of sufficient Cu-poorness for device relevance (i.e. $y \approx 0.9$). The $Cu(In,Ga)Se_2$ layers resulting from this process are found to be weakly (220)(204) oriented and present crevices of depths determined by the layer thickness grown in the third stage. It is hypothesized that these crevices result from the conversion of the Cu_xSe to $Cu(In,Ga)Se_2$ in the fourth stage of the growth, but they do not prevent the layers from device quality, at least at the 15 % level for less than 20 minute growths. Nevertheless, ideas are presented on possible ways to avoid this crevice formation and on the presented growth process.